MultiScatter: Multistatic Backscatter Networking for Battery-Free Sensors

Mohamad Katanbaf*
katanbaf@uw.edu
University of Washington

Ali Saffari*
saffaria@uw.edu
University of Washington

Joshua R. Smith
jrs@cs.washington.edu
University of Washington

ABSTRACT

Realizing the vision of ubiquitous battery-free sensing has proven to be challenging, mainly due to the practical energy and range limitations of current wireless communication systems. To address this, we design the first wide-area and scalable backscatter network with multiple receivers (RX) and transmitters (TX) base units to communicate with battery-free sensor nodes. Our system circumvents the inherent limitations of backscatter systems -including the limited coverage area, frequency-dependent operability, and sensor node limitations in handling network tasks- by introducing several coordination techniques between the base units starting from a single RX-TX pair to networks with many RX and TX units.

We build low-cost RX and TX base units and battery-free sensor nodes with multiple sensing modalities and evaluate the performance of the MultiScatter system in various deployments. Our evaluation shows that we can successfully communicate with battery-free sensor nodes across 23400 ^{2} of a two-floor educational complex using 5 RX and 20 TX units, costing $569. Also, we show that the aggregated throughput of the backscatter network increases linearly as the number of RX units and the network coverage grows.

CCS CONCEPTS

• **Hardware** *Sensor applications and deployments*; **Wireless devices**; • **Computer systems organization** *Sensor networks*; *Embedded systems*.

KEYWORDS

Backscatter, sensor platforms, energy harvesting, wireless sensor networks, Internet of Things, battery-free camera, battery-free microphone, battery-free sensor

---

*Both authors contributed equally to this research.

---

1 INTRODUCTION

Recent advances in energy harvesting, physical sensors, wireless networks, data processing, and machine intelligence picture a future where billions of everyday objects turn into smart, connected devices that can sense their surroundings, communicate their data, and react to human interactions and other environmental stimuli. This vision, however, has run into practical limitations of wireless communication networks.

An ideal wireless technology for a battery-free or self-powered sensor network should possess two essential qualifications: the sensor nodes should consume very little energy since the harvested energy is scarce, and the infrastructure to communicate with the sensor nodes should be low-cost to make widespread adaptation feasible. Current commercial wireless technologies do not satisfy these two objectives simultaneously. While recent works have demonstrated battery-free BLE [30, 81], Sub-GHz [37], and LoRa [61] networks, these radios may consume too much energy to support applications demanding update rates of multiple packets per second [85]. On the other hand, passive RFID readers are expensive and suffer from a short communication range, resulting in high infrastructure cost to cover a practical setting with passive RFID readers [28]. In addition, RFID does not typically support the use of arbitrary sensors such as cameras and microphones.

Recent bistatic backscatter systems [42, 46, 49, 70] have shown promise to find a middle-ground to this challenge by employing the backscatter technology to reduce the energy burden of wireless communication, while leveraging the economies of scales and ubiquity of industry-standard protocols such as WiFi, Bluetooth, ZigBee, and LoRa to reduce the cost of reader infrastructure. Bistatic backscatter systems still suffer from a shorter communication range than conventional active radios, and a single receiver (RX)-transmitter (TX) pair is insufficient to cover a multi-bedroom or multi-floor house at practical data rates. The limited coverage of backscatter systems complicates the user experience and limits their use cases.

To extend the coverage of a wireless network, the idea of using multiple base units is suggested and implemented in cellular [24, 71] and WiFi [29, 69] networks for a long time. However, high propagation loss, strong interference, frequency-dependant operation and non-homogeneous base units complicates the deployment of a backscatter network with multiple base units (see §2 for a primer on backscatter systems).

Furthermore, the battery-free sensor nodes have strict energy limitations, while the base units have higher computational and energy resources. This imbalance requires the system to push the network management tasks to the base units while keeping the sensor nodes as simple as possible.

We notice that unlike a cellular base station that covers a circle around itself, the coverage area of the bistatic backscatter system is
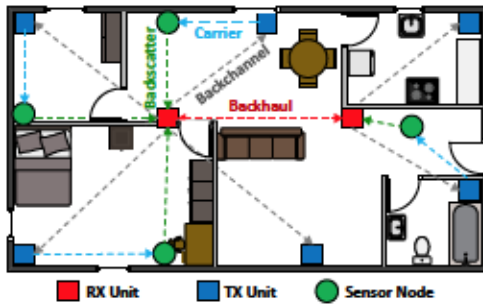
Figure 1: We deploy multiple RX (red squares) and TX (blue squares) base units and introduce several coordination techniques to extend the coverage of low-cost backscatter networks and deliver seamless connectivity to battery-free sensor nodes (green circles).

almost entirely limited to the area between the TX and RX units (see Fig. 2(a)). This difference means that we do not need another TX-RX pair to double the coverage area of a bistatic backscatter system. We only need to add a second TX unit and share one RX unit between the two TX units (or vice versa). We extend this idea of sharing TX units and RX units among one another, to form a multistatic network of many TX and RX units that covers more extensive areas, as shown in Fig. 1. This solution still uses backscatter to communicate with the sensor nodes, which reduces the energy harvesting barrier for a practical solution. Although this solution needs multiple base units similar to an RFID solution, each TX or RX base unit is significantly cheaper than an RFID reader.

1.1 MultiScatter

In this work, we present MultiScatter, the first multistatic backscatter network for battery-free sensing, where a network of multiple RX and TX base units is employed to deliver backscatter connectivity to many battery-free sensor nodes over a wide area. We extend the idea of bistatic backscatter with a single RX-TX pair to multistatic backscatter with multiple RX and TX base units, where any RX-TX pair can communicate with any sensor node in its vicinity. We introduce a MAC layer for the multiscatter backscatter network that performs two critical tasks: first, it selects the best RX-TX pair, carrier power, and frequency in communicating with each sensor node to maximize the throughput, and second, it handles the handover between base units as the sensor node moves inside the coverage area. This seamless connectivity addresses one of the remaining challenges in using backscatter systems and creates many new opportunities in smart homes and smart buildings by enabling peripheral, wearable, and medical devices such as pill bottles [64] and insulin pens [52] to use backscatter to transfer data to the cloud.

1.1.1 Summary of architecture. Fig. 1 shows the architecture of the system. The RX units manage the operation of the TX units and sensor nodes. We make this design choice since, unlike the TX units, the RX units have direct access to the backscatter channel state information.

The RX units support three different wireless communication interfaces. They can receive backscattered packets from the sensor nodes (dashed green line in Fig. 1). The RX units can also actively send packets to the TX units; we call this the backchannel link

(dashed gray line). The RX units use the backchannel link to activate the best TX unit for each sensor node and set TX parameters like carrier frequency and power. Finally, a backhaul link (dashed red line) allows RX units to communicate with other RX units to share network state information, including the sensor nodes' connection states.

The TX units support two wireless interfaces: they receive active packets from the RX units, and transmit the commands and carrier signal to the sensor nodes (dashed blue line).

1.1.2 Deployment design support tool. To handle the complex coverage scenarios of a multistatic backscatter system in indoor environments, we develop a deployment planning tool to assist us in finding the optimum placement of RX and TX base units. While using two different base unit types is a major factor in lowering the cost of backscatter infrastructure, it complicates the deployment. The backscatter coverage depends on several factors, including the carrier source power, receiver sensitivity, and receiver blocker tolerance [47], and the objects and obstacles in indoor environments further complicate the coverage of a multistatic backscatter system. Our tool takes into account the backscatter range equations, attenuation through obstacles in indoor environments, and possible base unit coordinates and suggests the best spots for RX and TX units.

1.1.3 Improved Power-Coverage-Data rate trade off. Our system design provides high data rate and wide coverage area for sensor nodes that power low enough to operate from harvested energy. The power reduction is achieved by using backscatter communication. Previous work has demonstrated battery-free microphones [84] and cameras [41, 78, 79]. However, these early results are not general: they relied on special-purpose analog modulation schemes that were custom designed for the specific sensor data. This work presents a general-purpose sensor node platform that can backscatter arbitrary digital sensor data as 802.15.4g-compliant packets. The demonstrated sensors include cameras and microphones, as well as sensors for temperature, humidity, and illuminance. Our sensor nodes are equipped with an ultra low power radio to wake them from sleep mode and receive commands. The sensor nodes can operate entirely on the energy harvested from a 2 ^{2} solar cell under indoor light intensity levels.

Previous long-range backscatter deployments such as [42, 70, 83, 87] used a single TX-RX pair and extended the communication range by using very sensitive, low data rate protocols. However, this technique is not scalable. The coverage area of one base unit has an upper limit, and one would need more than one base unit to extend the coverage beyond that. In this work, we provide wide area backscatter deployment coverage using a larger number of multi-statically defined small cells, which allows us to maintain higher data rates for the battery-free sensor nodes.

1.2 Contributions

Our main contributions are summarized below:

We present the first multistatic backscatter network for battery-free sensing. Our system relies on three different wireless links and uses several coordination techniques between the base units to deliver a high throughput seamless connectivity over a wide area

(a) Backscatter coverage dependence on the RX-TX distance.

(b) Multi-path fading experiment setup.

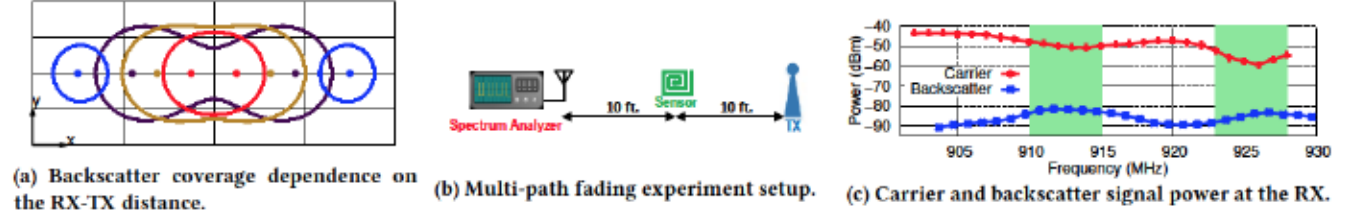(c) Carrier and backscatter signal power at the RX.

Figure 2: Backscatter coverage map (a). Effect of multi-path fading on backscatter link (b,c).

to battery-free backscatter sensor nodes. Our MAC layer implementation selects the best RX-TX pair in communicating with each sensor node to maximize the throughput and handles the handover between base units as the sensor node moves inside the coverage area.

• We develop a deployment planning tool to assist us in finding the optimum placement for RX and TX base units to maximize the coverage in indoor environments. Our tool considers the backscatter range equations, attenuation through obstacles in indoor environments, and potential base unit coordinates and suggests the locations for RX and TX units.

• We build the MultiScatter system, including the RX and TX base units, and sensor nodes and evaluate it in different scenarios. Our evaluations show that the MultiScatter can cover a $23400 ft^2$ educational complex using 5 RX units and 20 TX units for a total cost of $569. Furthermore, the aggregate throughput of the backscatter network increases by using more RX units. Using 5 RX units, our backscatter network collects data from multiple sensors at an aggregate rate of 375 Kbps, 4.17 times faster than a single sensor node throughput.

Platform availability. MultiScatter's design files are available at:

https://github.com/MultiScatter/Hardware

2 BACKSCATTER PRIMER

Unlike conventional wireless networks where the communication happens between two devices- an access point and a mobile device- three devices are involved in a bistatic backscatter communication; a TX unit that generates the carrier signal, a backscatter sensor node that modulates and reflects the carrier, and an RX unit that listens to, and decodes the sensor node data.

One of the main challenges in backscatter systems is the strong interference at the receiver due to the carrier signal. Bistatic, or half-duplex, backscatter systems rely on physical separation of the TX and RX units to reduce the carrier interference [46, 49, 83], while monostatic, or full-duplex, backscatter systems rely on self-interference cancellation circuits for this purpose [27, 33, 48]. Another popular technique to mitigate the carrier interference is using sub-carrier modulation at the sensor node [33, 43, 46, 48, 49, 83, 87, 92] to generate the backscatter packet at a frequency offset from the carrier signal. This technique pushes the carrier signal out of the desired band at the receiver and reduces the receiver's sensitivity loss, since receivers can tolerate out-of-band interference.

The coverage of a bistatic backscatter system depends on the relative distance of the RX and TX units and characteristics such as receiver sensitivity and blocker tolerance, transmitter output power, backscatter node conversion gain and antenna gain as described in [47, 49]. We use the signal propagation model to plot the

backscatter coverage in four different cases in Fig. 2(a). The RX and TX locations are shown with circles of the same color in each case. When the TX and RX are too close to each other, they completely cover the area between themselves, but the carrier interference limits the coverage area (red plot). As the RX-TX distance increases, the coverage area expands to reach its maximum (brown plot). If we further increase the RX-TX distance, first, the coverage width at the center starts to shrink (purple plot), and finally, we lose the coverage at the center and the coverage map becomes disjoint (blue plot). Although we use a hypothetical backscatter system and the free-space propagation model in this analysis, the coverage variation trend is similar in all bistatic backscatter systems, and it highlights the importance of RX and TX units placement in covering large spaces with backscatter connectivity.

The wireless propagation in indoor environments is subject to multipath fading. To show the effect of the multipath fading, we perform a simple experiment. We set a transmitter to generate a continuous wave carrier signal, and a backscatter node, placed 10 ft away from the TX, to reflect the TX signal at 1.7 MHz offset frequency, as shown in Fig. 2(b). We use a spectrum analyzer, placed 10 ft away from the backscatter node, to measure the carrier and corresponding backscatter signal powers. Fig. 2(c) shows the carrier and backscatter signal power as we sweep the carrier frequency from 902 MHz to 928 MHz. The backscatter (i.e., desired) signal power varies 10dB in this experiment, while the carrier (i.e., interference) signal power varies 15dB. The two signal powers are independent of each other, and their peaks and valleys happen at different frequencies. The best frequency bands for backscatter communication are the ones with maximum backscatter signal power and minimum carrier power as shown in Fig. 2(c) with green strips.

3 SYSTEM DESIGN

This section describes the backscatter network architecture used to cover a wide area and communicate with many sensor nodes. We start with one RX-TX pair and extend the coverage first by adding more TX units and finally by including more RX units. Throughout this section, we assume that each sensor node has a unique identification number (ID), and the backscatter network has prior knowledge of the sensor nodes' IDs.

3.1 Single RX - Single TX

In the simplest form, a bistatic backscatter system consists of one RX unit, one TX unit, and one or several sensor nodes. The RX and TX should coordinate with one another to achieve three main functionalities: improving the link reliability, time-frequency alignment, and handling retransmissions. We use a wireless backchannel between the RX and TX units to communicate and coordinate between the two devices.
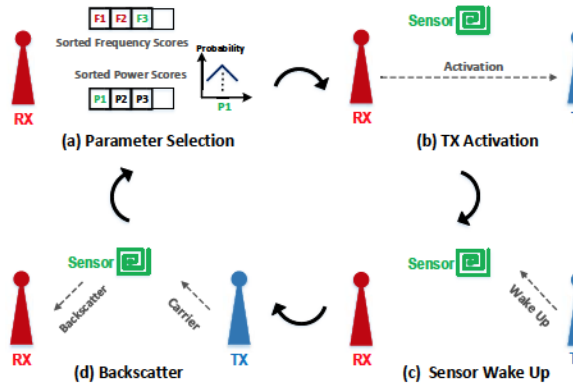
Figure 3: Proposed Communication cycle.

The communication cycle of the system is shown in Fig. 3. It starts with selecting the optimum parameters for the frequency channel and carrier power to maximize link throughput and minimize the error rate in communicating with the specified sensor node. The RX uses scores calculated based on the results of previous communication cycles for this purpose. The RX selects the frequency channel with the highest score that satisfies the frequency hopping requirements of the regulatory mandates. It also finds the carrier power with the highest success rate and uses it as the center of probability distribution to select the carrier power (Fig. 3(a)). After selecting the communication parameters, the RX shares them with the TX unit. The TX unit has been in listening mode until it receives an activation packet from the RX unit on the backchannel. The activation packet also specifies the duration of the carrier signal that the TX unit has to generate, as well as the sensor node identification number and the command for the sensor node (Fig. 3(b)). Once the TX unit receives the activation packet, it sends a packet to the sensor node, which contains the sensor node ID and the requested command, to wake the sensor node (Fig. 3(c)). Finally, the sensor node wakes up, receives the command, and responds appropriately by transmitting one or several backscatter packets. During this period, the TX generates the carrier signal, and the RX listens for the backscatter packets (Fig. 3(d)). When the backscatter duration is over, the RX unit analyzes the received packets based on the command issued to the sensor node and decides whether retransmission is required or not. It also updates the frequency and power score vectors based on the communication cycle results. The devices follow the same cycle for the subsequent communications between them.

The first step of the communication cycle is to select backscatter frequency and power level. This step is vital to improve the overall throughput and reliability of the system since backscatter and carrier signal strengths at the receiver vary significantly at different frequency channels due to the multipath in indoor environments, as mentioned in Sec. 2. Similarly, the carrier power could affect the performance of the backscatter communication too. Increasing carrier power increases both the backscatter signal power and TX carrier interference at the RX unit at the same time, and might improve or deteriorate the performance of the backscatter link [47]. We assign a success score to each communication cycle based on

the ratio of the successfully received packets to the total expected packets, and update the score for the frequency channel and power level used in the cycle with a moving average formula. To explore the entire space of possible frequency and power values, we set an exploration probability based on the error rate over a predefined number of previous communication cycles. In exploration mode, we select the two parameters randomly [46].

The communication cycle allows the RX unit to control the TX carrier frequency, start time and duration through the activation packet. This control is essential for two reasons. First, the TX unit can not generate the carrier signal indefinitely since it would waste energy and generate too much interference for other wireless users in the vicinity. The TX unit should only generate the carrier when required by the sensor node, which means the devices should be time-aligned to utilize the spectrum and energy resources efficiently. Furthermore, the TX has to hop between different frequencies in the ISM band to satisfy regulatory mandates [9]. Since the desired signal frequency at the RX is equal to the TX frequency plus the subcarrier modulation frequency of the sensor node [46, 49, 83], the RX needs to know these two values in order to frequency align itself with other devices. Using the activation packet to initiate and control the TX operation guarantees time and frequency alignment between the devices.

In the proposed communication cycle, the RX unit sends the sensor node command to the TX unit, and the TX unit passes the command to the sensor. Thus, the data communication effectively happens between the RX unit and the sensor, with the TX unit facilitating the data transfer between them. The two base units have different capabilities in a bistatic backscatter network. The RX unit demodulates the backscatter signal and detects whether the desired packet is successfully received or failed, and the TX unit can communicate with the sensor node. By using the TX unit as a relay, the RX unit has complete control to ask for retransmissions.

3.2 Single RX - Multiple TX

The system described in Sec. 3.1 highlights the fact that the data exchange happens between the RX unit and the sensor nodes. Thus, adding more TX units to the system improves the backscatter system coverage without significantly affecting the system architecture. One approach to developing such a network with multiple TX units is to command all units simultaneously to generate a carrier signal at a specific frequency. However, this method faces two major challenges: first, using multiple transmitters would not guarantee better performance because signals from different transmitters might combine destructively and decrease the backscatter signal power at the receiver. Second, it would increase the system energy consumption and interference to other wireless systems in the vicinity. Thus, the communication system must select one TX unit for each communication cycle to maximize the throughput. We use the RX unit to control the system's operation and set the TX unit at the start of each cycle.

To compare the performance of different TX nodes in communicating with each sensor node, we assign a confidence score to each TX unit. The confidence scores are initialized to 1 and updated with an exponential moving average formula using the cycle success rate each time the TX unit-sensor node combination is used.
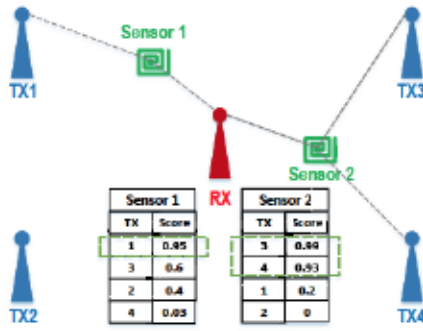
Figure 4: TX unit selection in a single RX - multiple TX scenario based on assigned confidence scores.

Fig. 4 shows sample confidence tables in the single RX - multiple TX arrangement for two sensor nodes. The frequency and power score vectors depend on the geometrical placement of the devices with respect to each other and change based on the selection of the TX unit. Thus, the RX unit needs to record one set of these score vectors for each TX unit-sensor node combination.

We follow the following procedure to select a TX unit based on the confidence table at the start of the communication cycle. First, we select the TX units with confidence scores higher than 0.9. If the set has more than one member, we use a weighted random selection to select one of them. If the set has no member, we filter out the TX units with confidence scores less than 0.2 times of the maximum confidence score, and use a weighted random selection to select one of the remaining TX units. Once the TX unit is selected, we follow the communication cycle, as explained in Sec. 3.1, with the selected TX unit. We assign a unique ID to each TX unit and include the transmitter ID in the activation packet.

Similar to the single RX-single TX architecture, the TX units are in listening mode until they receive the activation packet. The TX units only move forward with transmitting the carrier if their ID is matched to the one in the activation packet. Otherwise, they discard the activation packet and return to the listening mode.

3.3 Multiple RX - Multiple TX

Increasing the number of TX units around one RX unit allows us to expand the backscatter coverage around the RX unit in different directions. However, we can only achieve a truly scalable system and cover areas beyond the reach of a single RX-TX pair by employing more than one RX unit. In the Multiple RX - Multiple TX arrangement, we break the area that we need to cover into several sections and use one RX unit with one or multiple TX units to cover each section. Similar to cellular networks, a sensor node might move between these sections. Since the backscatter sensor nodes do not have the hardware or energy resources to determine the link quality metrics, the base units have to handle the handover. We add a server role to the network that assigns the sensor nodes to the RX units and updates these assignments as the sensor nodes move. The server could be one of the RX units, or a separate device. We equip the RX units with WiFi and use it as the backhaul link to communicate with the server.

Once a sensor node moves from section A to section B, we need to change its assigned RX unit. For this purpose, first, the RX_A must alarm that the sensor node is missing, and then, the RX_B must search for the sensor node and successfully communicate with it. A sensor node could move to any other section between two communication cycles in a backscatter network, since the sections are small and the time interval between communication attempts could be long.

We use the number of consecutively dropped packets as the metric to detect a sensor node is disconnected from its assigned RX unit since once a sensor node leaves a given section, all backscatter communication attempts with that sensor would fail.

We define the re-assignment cost ($Cost_{RA}$) as the average number of communication cycles that the system needs to correctly assign a new RX unit to a relocated sensor node. We can calculate the re-assignment cost in number of communication cycles using equation 1:

$$Cost_{RA} = (Thr_{drops} + 0.5 \times N_{TX} \times N_{ch}) \times (\frac{1}{1 - PFA}) \ (1)$$

where Thr_{drops} is the threshold for consecutive dropped packets that is used to flag a missing node, N_{TX} is the number of TX units in the network, N_{ch} is the number of communication cycles that an RX-TX pair needs to search for the sensor node, and PFA is the probability of false alarm. There is a trade-off in selecting the threshold to announce the disconnection to the server. Higher thresholds waste network resources by trying to communicate with a sensor node that has left the section. On the other hand, lower thresholds increase the probability of false alarm. To select the optimum threshold that minimizes the cost, we need to know the N_{ch} for a reliable search procedure and model the probability of false alarm at different Thr_{drops} values.

Search Procedure (N_{ch} selection). An ideal search procedure should be fast and accurate. Due to the lack of existing knowledge about channel properties, the RX units have to try different frequency channels to increase the likelihood of successful communication with the sensor node at the new location. However, increasing the number of frequency channels in the search procedure would increase the search duration (N_{ch}). Previous studies [50, 54] show that the multipath fading loss in indoor environments becomes uncorrelated as the frequency separation increases. To find the optimum number of frequency bands for the search procedure, we set up TX-RX base units at 12 different locations with 20 sensor node testing points (240 total) around them. For each setup, we set the carrier power at the maximum and try all the frequency bands between 902 MHz and 928 MHz with 400 KHz channel spacing to communicate with the sensor node at each point.

Fig 5(a) shows the distribution of number of operative bands over the 240 points, with 35% of the points not responding at any frequency and 13% of the points responding at all of them. We consider the points which respond at least at 10% of the frequency bands (150 points) as the target group and plot the probability of communicating with the sensor at these target points based on the number of attempted frequency channels in Fig 5(b). The figure shows that trying 9 channels results in 99% search accuracy. We consider some margin for errors in these experimental results and
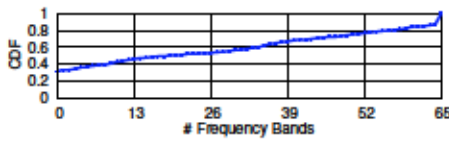
(a) Distribution of number of operative bands at 240 locations.
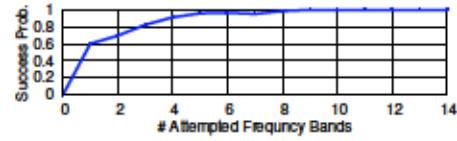
(b) Probability of communication with a sensor node based on number of equal-distant frequency bands attempted.

Figure 5: Selecting the number of frequency bands for the search procedure.

use 12 equally spaced frequencies in our search routine, which means the search procedure takes 12 commutation cycles.

Threshold Selection. The probability of false alarm   is the ratio of false alarms to total alarms. The main cause of successive dropped packets that leads to a missing node alarm is the movement of the sensor nodes. Ideally, we would like the RX unit to generate an alarm only when the sensor node is moved to a different section. However, moving the sensor within the boundaries of a section could result in multiple consecutive dropped packets, too, since the RX units have to re-tune the score vectors for the new sensor location as described in Sec. 3.1. This further complicates the threshold selection. We can calculate the false alarm rate using equation 2:

$$\tag{2}$$

where   and   are the probability of a sensor moving inside and outside of a given section respectively, and the   and   are the probability of generating an alarm as a result of those moves. Based on our definition, any alarm generated when the sensor moves outside the section is true, and hence,   is equal to zero. Also, we assume an 80%-20% split between the probabilities of moving inside and outside a section. Thus, to estimate the   , we must model the probability of false alarm caused by moving a sensor inside a section for different thresholds.

We perform an experiment by moving the sensor node within the boundaries of one section 100 times in 5 different environments. Fig. 6 (blue line) shows the probability of generating an alarm for different thresholds in these experiments. If we apply these probabilities to equation 2 and assume   and   are equal to 10 and 12 in equation 1, we can calculate the re-assignment cost for different threshold levels as shown in Fig. 6 (red line). Based on this plot, the optimum threshold of consecutive dropped packets for a system with 10 TX units is 22 packets.

Server. The server tracks the assigned RX unit for each sensor node. Once one of the RX units detects a missing sensor, it notifies the server. The server then randomly notifies one of the other RX units to search for the missing sensor node and waits for the search result. If the search fails, the server notifies another RX unit, and this procedure continues until one of the RX units successfully communicates with the sensor node. The server holds a predefined period before notifying the same RX unit again.

3.4 Base Units Placement

Selecting the number of base units to cover an area and finding their optimum placement could be challenging, especially in residential and commercial buildings, which are the primary target of the MultiScatter system. Thus, we need a tool to help us plan the deployment and estimate the coverage area for a given placement
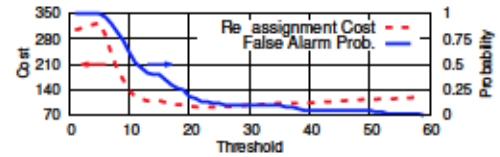

Figure 6: Probability of false alarm (blue) and the overall re-assignment cost in communication cycles (dashed red) for different consecutive dropped packets thresholds.

of base units without the time-consuming process of deploying the units in the field. Although several RF propagation simulators are available [20, 21], to the best of our knowledge, none of them supports backscatter systems.

Several factors complicate the placement of base units in indoor environments. First, the coverage of a single RX-TX pair of our multistatic network is a complex function of the RX-TX relative distance, as shown in Fig. 2(a), as well as other factors such as TX carrier power, RX sensitivity, and blocker tolerance [47]. Furthermore, indoor areas are most often divided into several sections by walls, partitions, or other obstacles. The RF signals attenuate as they pass through different materials. It is essential to consider the effect of these obstacles in the placement of the RX and TX units to achieve optimal performance. Finally, the base units have high energy consumption and need a permanent energy supply such as a wall power outlet. This adds another limit to the placement of the base units since we prefer to keep the base units closer to the wall power outlets and avoid long wires.

Our tool uses the Friis formula [35] to estimate the backscatter signal and carrier interference power levels at the receiver. We use the backscatter coverage equations in [47] to determine the backscatter coverage at each point in the environment. We estimate the attenuation through walls and other obstacles using the proposed models in [25, 26, 75]. Although our simulator is limited to path loss and absorption loss models in two dimensions and does not consider RF propagation effects such as reflections, diffraction, and scattering, it still provides valuable insight for placing the target area's base units.

Our deployment tool takes the geometry of the area and coordinates of the base units as the inputs and calculates the maximum backscatter signal power amongst all the RX-TX pairs at each point to generate a coverage map. We follow a manual trial-and-error process to find the number and position of the base units required to achieve the desired coverage. In each iteration, we move the base units and add more units, if needed, to get the desired coverage. More enhanced features, such as automatic placement of the base units to achieve defined coverage goals, are left for future work. We can use a hard threshold coverage function that outputs one when backscatter signal power is above RX sensitivity and the carrier
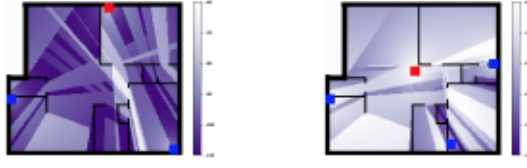
(a) One RX and two TX units   (b) One RX and three TX units

Figure 7: Simulating the backscatter signal power for a two-bedroom apartment using the deployment planning tool.

interference is below the RX blocker tolerance, and zero otherwise, or a soft threshold coverage function that transitions smoothly between zero and one.

We use our simulator to plot the backscatter signal power in a 900 ^{2} two-bedroom apartment unit in two different cases, a single RX - two TX (Fig. 7(a)), and a single RX - three TX (Fig. 7(b)) configurations, where a brighter color shows a stronger backscatter signal power. In this simulation, we assume all devices use antennas with 0 dBi gain, and frequency band, carrier power, backscatter conversion loss, path loss exponent, and attenuation through internal walls are equal to 915   25   4   2 and 15 , respectively. The results clearly show that adding one more TX unit and placing the base units appropriately have a significant effect on the performance of the MultiScatter system.

During our evaluations (Sec. 6), we notice that placing the base units closer to walls or other large objects could improve backscatter performance. The strong multipath resulted from such large objects could help the backscatter systems by creating a frequency-dependent non-flat attenuation profile, resulting in enough operative frequency bands for backscatter communication. Improving the simulator to model these higher-order effects and creating a more accurate coverage map is left for future work.

4 SENSOR NODE DESIGN

Our goal is to design a battery-free sensor node platform that can accommodate different sensors and communicate with the base units. We reduce the wireless power consumption of the sensor node by using low-power backscatter for the sensor node uplink and an ultra-low-power wake-up radio for the sensor node downlink. The wake-up radio allows the sensor node to stay in idle mode until the base units activate it. We also implement a gating technique to reduce the energy burden of power-hungry sensors by adding low-power auxiliary sensors. For example, a motion sensor is used to gate the operation of the camera. Finally, we use a low-power micro-controller with several communication protocols in our sensor node platform, which can interface with various commercial sensors.

FSK Backscatter. The sensor node transmits the data to the RX unit using Frequency-Shift Keying (FSK) backscatter communication. In FSK backscatter, bits '0' and '1' are transmitted by changing the state of the RF switch connected to the antenna at frequencies $_0$ and $_1$. This results in a backscatter packet with $_0$ $_1$ 2 subcarrier modulation and $_0$ $_1$ 2 frequency deviation.

We use a temperature-compensated VCO to generate the variable frequency signal that controls the RF switch. We use two NMOS switches to control the resistor that sets the oscillator frequency, as shown in Fig. 8. Switch Q1 controls the backscatter subcarrier
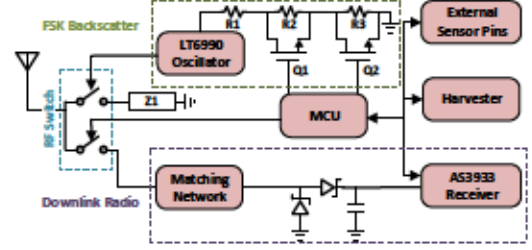

Figure 8: Sensor node block diagram.

modulation frequency, and switch Q2 sets the transmitted bit to '1' or '0'. We use the micro-controller SPI interface derived by the MCU oscillator to generate accurate bit periods. Compare to using two individual oscillators to generate $_0$ and $_1$ frequencies [87], using a single controlled oscillator to generate both frequencies reduces the power consumption and ensures phase continuity in switching between the two frequencies.

Low Idle Power Consumption. The sensor node operates in the idle mode until it is activated by the base units to enable one of its sensors or report its latest recorded data. Therefore, our sensor nodes must be power efficient in the idle mode. Although the FP-GAs allow us to implement custom communication protocols, they consume more power in the idle mode than the MCUs. We use a low-power MCU with several low-power idle modes in this work.

To wake up the MCU from the idle mode, we use a low-power and low-frequency wake-up radio [46]. While the MCU is in the idle mode, the wake-up radio listens to the packets transmitted by the TX units. If the received packet matches the sensor node's 16-bit ID, the radio generates an interrupt to the sensor node MCU and passes the received command to it.

Sensor Gating. We use low-power auxiliary sensors to gate the operation of the power-hungry sensors. For instance, a motion sensor can enable the operation of an image sensor when there is movement in the room. This helps us reduce the power consumption of the sensor node by limiting the operation of the power-hungry sensor (image sensor) to informative events. Similarly, the microphone activates only when the sound intensity passes a defined threshold.

We also implement second gating criteria by monitoring the energy storage element of the sensor node. The MCU measures the voltage of the energy storage element and sends it back to the base units in response to each sensor enable command. The base units monitor this voltage and use it to gate the commands issued to the sensor node. If the voltage falls below a defined threshold, the base units bypass the sensor reading requests from that sensor node and allow the energy harvesting unit to charge the storage element. The base units continue to monitor the energy storage voltage with a more extended reading period and resume regular operation once the voltage reaches a certain level.

Energy Harvesting and Storage. The energy harvesting unit of the sensor node collects energy from ambient light and stores it on an energy storage element. The energy storage element connected to each sensor node should store enough energy to support reading the physical sensors connected to the sensor node and transmitting their data to the base units. While supercapacitors have longer life cycles and can be employed to build truly battery-free sensor nodes, rechargeable batteries have higher energy capacity and can tolerate

longer energy drought periods [72, 93]. Our energy harvesting unit can work with both types of energy storage elements.

Modular Design. We follow a modular design approach to building our sensor nodes. The MCU, wireless communication units, temperature, humidity, and illuminance sensors are placed together as the basic sensor node. The energy harvesting unit, camera, and microphone sensors are designed as add-on boards that mount on top of the basic sensor node through 5 power and 12 Input/Output (IO) pins (see Fig. 9(c)-(e)). The modular design allows us to support more sensors without redesigning the communication section.

5 IMPLEMENTATION

We implement MultiScatter, consisting of the RX base units, TX base units, and sensor nodes, for operation in 902-928 MHz ISM band on 4-layer FR4 PCB. The system uses FSK modulation and 802.15.4g packet structure with seven preamble bytes, 16 CRC bits, and no whitening for communication between devices.

5.1 Base Units

Receiver Units. The RX unit has two parts, a communication board with the CC1352R [16] wireless MCU, and a Raspberry Pi 4B single-board computer (RPi) with 2GB RAM for processing and backhaul. The two boards are connected to each other, as shown in Fig. 9(a), and communicate through a 1Mbps serial link. The CC1352R supports FSK modulation with data rates from 0.3 to 1985 Kbps and RX filter bandwidths from 4.3 to 3767 KHz. The RX filter bandwidth determines the carrier attenuation and should be set accurately considering the data rate, frequency deviation, and subcarrier modulation frequency. Our CC1352R board consumes 30 mW for its operation on average. The RPi board runs the Raspbian operating system. It processes the received data from the sensor nodes and determines the activation packet parameters. The RPi sends out this information to the CC1352R MCU to start the communication cycle, and the CC1352R MCU passes the received backscatter packets to the RPi as they are received. We implement the data handling and communication protocols explained in Sec. 3 using Python 3.7, which runs on the RPi.

Transmitter Units. Each TX unit consists of a CC1312R [15] sub-GHz wireless MCU that receives the activation packet and generates the carrier signal, and a SKY65313-21 [7] power amplifier (PA) that amplifies the carrier signal up to 28 dBm. Our TX unit consumes up to 3.3 W while transmitting carrier at 28 dBm and its ground planes distribute the heat generated by the PA to limit the PA surface temperature to 65 . Fig. 9(b) shows the fabricated TX unit.

Server. One of the RX units also handles the server tasks. We use the python socket.io protocol [19] to handle the communication between the RX units and server.

Data Collection Scheduling. The data collection process from each sensor initiates when the sensor node marks the availability of new data or when a pre-defined timeout is reached. The data collection might take one or several iterations. At each iteration, the RX unit first checks all the ongoing data collection processes for completion. If a portion of the data is missing, the RX unit generates the commands to read the missing parts and stores them in a queue. Next, all the commands in the queue are executed, and
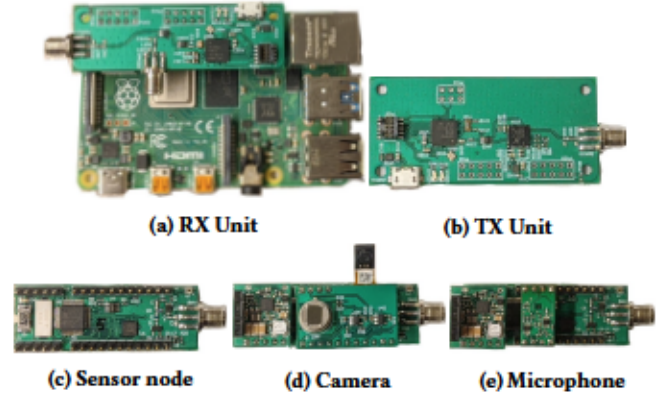

(a) RX Unit (b) TX Unit

(c) Sensor node (d) Camera (e) Microphone

Figure 9: Prototype hardware.

the responses to each command are processed. Once the queue is empty, the iteration is completed. We use time-division multiple access to accommodate multiple sensor nodes. Each sensor node has a unique ID, and only one sensor node responds to the command from the RX unit at each cycle.

Cost Analysis. We design MultiScatter intending to reduce the infrastructure cost of a wide area backscatter network. Our analysis using pricing data from Octopart [22] shows that at low volumes of 1,000 units, the TX and RX base units cost $16.1 and $49.6 (including $35 for the RPi), respectively. The number of base units required to cover a specific building depends on its floor plan. We provide two sample cases in Sec. 6.

5.2 Sensor Node

We select STM32L071C8 [12], an ultra-low-power ARM Cortex-M0+ MCU with 20 KBytes RAM, as the sensor node MCU. The memory capacity is enough to store one image frame or one second of audio recording. A 4 MHz external crystal generates the MCU clock. We use AS3933 [4] wake-up radio for downlink, and LT6990 [17] VCO for generating the backscatter uplink signal. The sensor node is also equipped with HDC2080 [10] humidity and temperature sensor, and opt3002 [6] ambient light sensor. The sensor node is powered up using a 2.5 V regulator. We set the MCU core voltage to 1.2 V to reduce its power consumption. The antenna is shared between the wake-up-receiver downlink and backscatter uplink via the AS213-92LF [2] RF switch, as shown in Fig. 8. A 47pF capacitor is chosen for 1 (see Fig. 8), which has a small impedance at the carrier frequency.

The sensor node supports four uplink data rates, 31.25 Kbps, 62.5 Kbps, 125 Kbps, and 250 Kbps. We use 1 MHz subcarrier modulation with 25 KHz frequency deviation for the two lower data rates, and 1.79 MHz subcarrier modulation with 80 KHz frequency deviation for the two higher data rates, by setting the values of R1, R2 and R3 to 26 7 , 22 1 and 2 5 , respectively.

In each communication cycle, the sensor node receives a one-byte command from the base units. Some commands invoke an action, such as taking a picture, while others request specific information, such as a portion of the recorded image. The sensor includes the received command in its response to the base units for verification.
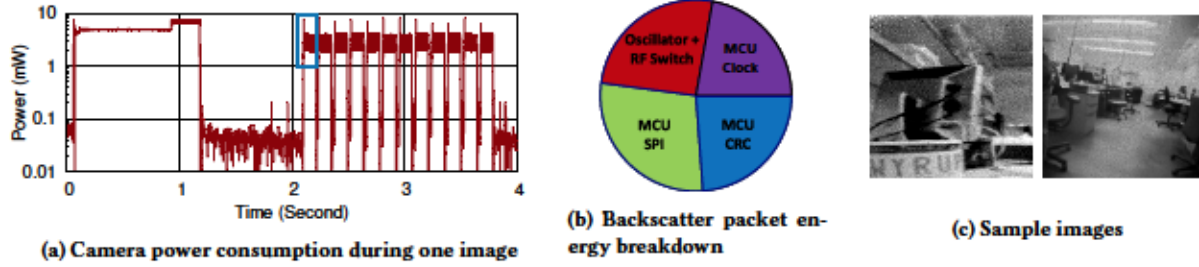
(a) Camera power consumption during one image

(b) Backscatter packet energy breakdown

(c) Sample images

Figure 10: Battery-free camera evaluation results.

Energy Harvester. We design the energy harvesting unit with the BQ25570 IC [8]. We use AM-1801 and AM-1816CA solar panels, designed for indoor operation with areas of 2 ² and 17 ² respectively [18], to supply the energy harvester board. The energy harvested from the solar cells is stored on a 100 mF super-capacitor [14] to support sensors such as a camera and a microphone.

Camera. We use a Himax HM01B0 image sensor [11] running in 120 120 QQVGA mode as the main sensor, and a Panasonic EKMB1104111 motion sensor [3] as the auxiliary gating sensor. Once the motion sensor is activated, or a take-picture command from the base unit is received, the MCU turns on the image sensor and enables its internal Phase-Locked Loop (PLL) to generate a 3 MHz clock for the image sensor. Once an image is captured, we turn off the motion sensor to avoid image overwrite and inform the base unit that an image is available. For data transmission, we divide one image into 12 large sections or 120 small sections, and the base unit can request a large or small section with a dedicated command to complete reading the image. Once the base unit successfully receives the image, it re-activates the motion sensor.

Microphone. Our microphone board is designed with a VM1010 microphone sensor [13]. The microphone has two operational modes, wake-up sound mode, and normal mode. In wake-up sound mode, which we use to gate the normal mode, it waits for an acoustic event to trigger the normal mode. The microphone records data for 1 second at 8 KS/s in normal mode. Transition between gating and normal modes and data transmission are similar to the camera.

Size and Cost Analysis. While we use commercial-off-the-shelf components to build our sensor node, recent works on integrated energy harvesters [32, 74], wake up radios [63, 77], and backscatter radios [89] clearly show the feasibility of integrating all electronics sections of our backscatter sensor node in an ASIC to significantly reduce its size and cost. In this case, the sensor node cost and size would be limited by the energy harvesting (i.e., solar cell) and the energy storage (i.e., supercapacitor) elements. In this work, we use a 100 mF supercapacitor to support sensors such as cameras and microphones. However, a 3 2 2 5 47 F capacitor stores enough energy to read the low-power sensors such as temperature and humidity sensors and transmit the data via a backscatter packet 3 times. Furthermore, recent advances in solar cell design [65] have shown 4 5 energy harvesting efficiency under indoor lighting conditions compared to the solar cells used in this work, which means a 0 45 ² solar panel would generate enough energy to power up our sensor node.

Energy Efficiency. The sensor node consumes 2 26 while transmitting backscatter packets, which is comparable to the commercial Sub-GHz active radios. However, we should note that this prototype is built with COTS components, while the commercial active radios are specifically optimized for low-power operation. Our evaluation in section 6 shows that the MCU consumes 74% of the energy in backscatter mode, which highlights the vast potential for improving energy efficiency by designing backscatter ASICs.

6 EVALUATION

We perform several experiments to demonstrate the performance of the MultiScatter system. First, we measure the power consumption of the sensor node with the camera module and evaluate the maximum sensor update rates using two solar cells with different sizes. Next, we evaluate the communication range of our system in line-of-sight and demonstrate the scalability of our solution in covering a two-floor educational complex. We verify the accuracy of our planning tool by comparing its outputs with measurements taken in an apartment unit. Also, we examine how deploying multiple RX and TX units affects the achievable aggregate throughput of the system. Finally, we show the handover performance when sensor nodes move in the network. We use omnidirectional whip antennas [1] for all devices in our evaluations.

6.1 Power Consumption

We evaluate the sensor node power consumption using the camera module since it is the most power-hungry sensor. Our setup consists of one RX-TX pair and a sensor node operating at 250 Kbps. Fig. 10(a) shows the measured power that the camera consumes while capturing and transmitting one image.

The operation of the camera starts in the idle mode, where it consumes 39 W on average. At time = 0.06 second, the sensor node is activated to take a picture and transfer it to the MCU. This process takes 1.2 second, and the average power is 5.04 mW. MCU PLL operation at the start and end of the process causes peaks in the power plot. Next, the RX unit requests transmission of the first section of the image, marked with the blue rectangle in Fig. 10(a), at time = 2.1 second. This is followed by requests for transmission of the other 11 sections to complete the picture. The image transmission takes 1.69 second, and the average power during this time is 2.26 mW.

Fig. 10(b) breaks down the energy that the sensor node consumes in transmitting a 38 byte backscatter packet. The MCU core consumes 23.8%, and 28.3% of the total energy (4.21 J) during CRC calculation and data transfer, while the MCU clock accounts for

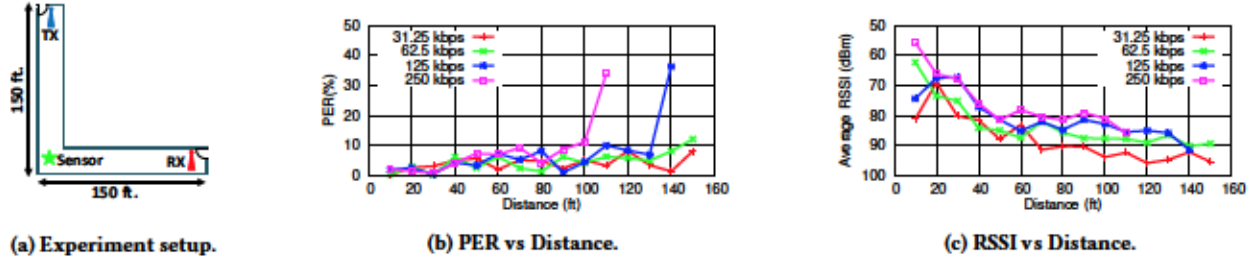(a) Experiment setup. (b) PER vs Distance. (c) RSSI vs Distance.

Figure 11: Line-of-sight communication range.

another 22.2%. The LTC6990 oscillator plus the RF switch consume the remaining 25.7%. In our prototype, the MCU consumes three-quarters of the total energy in backscatter mode, highlighting the vast efficiency potentials in designing custom ASICs for backscatter sensor nodes.

Fig. 10(c) shows sample images captured by battery-free camera.

6.2 Energy Harvesting

We use AM-1801 and AM-1816CA solar panels to supply the energy harvester board and evaluate the battery-free sensor nodes update rates. We set up the solar-powered sensors in an office building with fluorescent ceiling lights. The illuminance at the surface of the solar cell is 300 lux. We record data for 6 hours using each solar panel and sensor. Table 1 lists the achieved average update rates using each solar panel, as well as the idle power consumption, sensing energy, and communication energy for each sensor. Our evaluation shows that the sensing energy is 62%, 56%, and 65% of the total consumed energy for the camera, microphone, and environmental sensors, respectively, which shows that the sensing energy is the most power-consuming part of the sensor and limits the sensor nodes update rate.

The 2 ^{2} solar cell can provide enough power for the operation of the camera and microphone sensors every 280 and 268 seconds. This is made possible by reducing the sensor node power consumption in idle mode using the gating sensors. We can increase the camera and microphone update rate to 17 and 11 seconds by using the larger solar panel. The sensor node 100 mF super-capacitor stores enough energy to transmit 21 images or 36 seconds of audio with a single charge (3.6 v-4.5 v).

The small solar cell supplies enough energy to read the environmental sensors, which include the temperature, humidity, and illuminance sensors, every second. The system in [5] uses the CC2650 wireless MCU to read a temperature and humidity sensor and transmit the result via a BLE packet. The evaluation in [5] shows that the setup consumes an average of 4.04 mA from a 3 v battery over 30 ms which results in a total energy consummation of 363.3 J per measurement transfer. This energy includes the energy required to wake the MCU from the low-power mode, communicate with the sensor, activate the radio, and transmit the data. In comparison, our sensor node consumes 39 J per measurement transfer, which is 9 lower than the BLE packet transfer implemented in [5].

6.3 Range

We set up the system in a 300 5 ft hallway with floor plan shown in Fig. 11(a) to evaluate the communication range of the Multi-Scatter system in line-of-sight. The sensor node is in the middle of

Table 1: Power consumption measurements for camera, microphone, and environmental sensors.

Measurement		Cam.	Mic.	Env.
Idle Power (W)		39	51	25
Sensing Energy (mJ)		6.05	3.51	0.025
Communication Energy (mJ)		3.82	2.84	0.014
Solar-Powered	2 ^{2}	280	268	1
Update Rate (Sec.)	17 ^{2}	17	11	0.2

the hallway (indicated with the green star). In each measurement, we place the RX and TX units at the same distance from the sensor node and measure the Packet Error Rate (PER) of backscatter communication over 1000 packets. We place the sensor node at the same distance from TX and RX units since it is the most challenging setup in backscatter deployments [45, 47]. If the sensor is placed closer to one base unit, the other base unit could be placed further away while maintaining the same PER. Fig. 11(b) shows the PER for four data rates as we increase the RX and TX distances from the sensor node, from 10 ft to 150 ft. Our results show that the MultiScatter system can operate up to 150 ft (length of the hallway) at the data rate of 31.25 Kbps (PER < 10%) with an average RSSI of -95 dBm. The maximum achievable range reduces to 100 ft when the sensor node transmits data at 250 Kbps with the RSSI of -80 dBm.

Fig. 11(c) shows that the RSSI values at 10 ft for 31.25 Kbps and 62.5 Kbps data rates are less than the next several measuring points, although the distance is increasing. This happens due to the carrier power tuning in the MultiScatter system, as explained in Sec. 3.1. At this short distance between the devices, the backscatter link achieves low PER with lower carrier power.

6.4 Coverage

To evaluate the performance of MultiScatter in a non-line-of-sight scenario, we set up the system in a two-floor educational complex, covering multiple rooms separated by glass and wood doors, as well as concrete walls, with a total area of 23400 ^{2}. Fig. 12(a) and (b) show the floor plan of the ground and first floor of the building. In our setup, we have 5 RX units (red squares) placed at the height of 3 ft from the floor, and 20 TX units (blue squares) attached to the concrete walls at 6 ft height. This combination of base units costs $569 at low volumes based on our cost analysis (see Sec. 5). We place the sensor node at 5 ft height and move it between 130 test points (green circles), while it communicates with the base units at 125 Kbps. The sensor node transmits 1000 backscatter packets at each test point, and we measure the PER and RSSI of the backscatter packets. Our results show that all test points have PER less than 15 %,
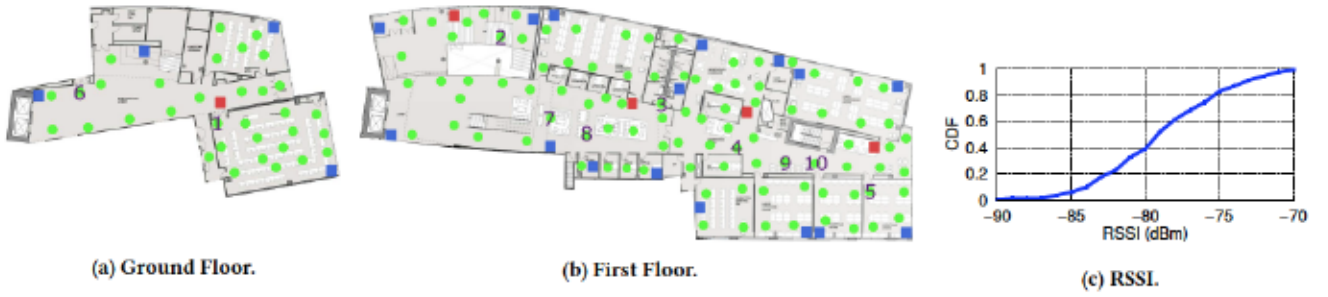
(a) Ground Floor. (b) First Floor. (c) RSSI.

Figure 12: Backscatter coverage in a two-floor educational complex. RX units, TX units and tested sensor node spots are shown with red squares, blue squares and green circles, respectively.

(a) Floor plan (b) 1 RX unit - 1 TX unit (c) 1 RX unit - 2 TX units (d) 1 RX units - 3 TX units
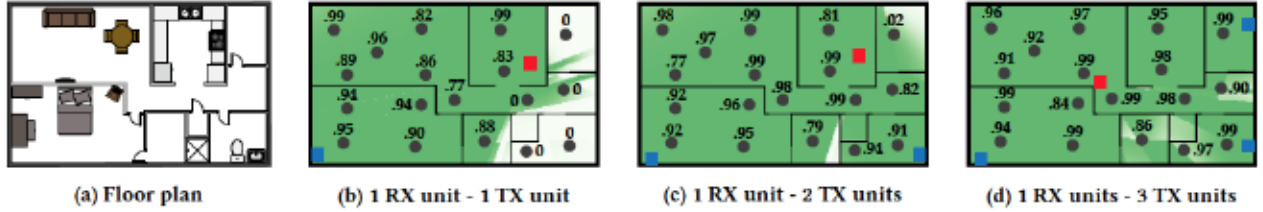
Figure 13: Verifying the planning tool in a single bedroom apartment coverage. The simulated coverage map, shown in green in three different cases, is a close estimate of the measured PER results at 18 different points around the apartment.
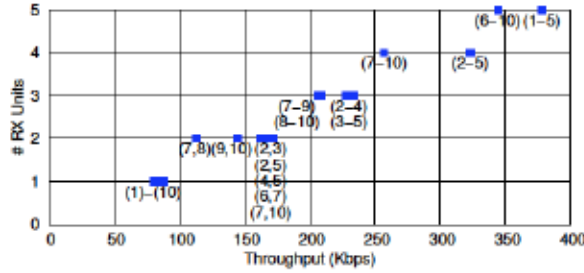

Figure 14: Aggregate throughput with multiple RX units.

and the median of RSSI is -77 dBm (Fig. 12(c)), which demonstrates that our system is fully capable of covering the entire building.

Also, we evaluate the performance of MultiScatter in a 34.5 $ft \times$ 21 ft single bedroom apartment (Fig. 13(a)). We use our deployment planning tool to determine the location of base units. To verify our tool model, we repeat the experiment using one RX unit and one to three TX units. In each test, we move the sensor node to 18 points around the apartment and calculate the PER over 500 packets. Fig. 13(b)-(d) show the simulated backscatter coverage using a soft threshold coverage function, where the darker points have a higher chance for successful backscatter coverage. The measured PER at each of the selected points is also specified in the figures. Our experiment results verify that our planning tool is a close estimate of the measured coverage.

6.5 Throughput

We deploy 5 RX, 20 TX, and 10 sensor node units operating at 125 Kbps in the building shown in Fig. 12 to evaluate the performance of MultiScatter in a multi-RX multi-TX scenario. The RX and TX units are placed as shown in Fig. 12(a) and (b), while the sensor node location is shown in the same figures with numbers 1 to 10. In this experiment, we assign two sensor nodes to each

RX unit, select a subset of the sensor nodes with 1 to 5 members, command them to transmit data to their assigned RX units, and measure the achieved data rate at each RX unit. To calculate the aggregate throughput, we add up the individual throughput of all RX units involved. Each point in Fig. 14 shows the results of one measurement, where the numbers in the parenthesis indicate the location of the sensor nodes involved in the measurement.

Our results in a single RX setup show that the maximum achievable throughput using one sensor node is 90 Kbps. All sensor nodes achieve a throughput close to this nominal data rate when they operate alone. Comparing the nominal data rate to the physical data rate of 125 Kbps shows a 28 % overhead. Our analysis shows that 10 % of this overhead is caused by the TX activation and sensor wake up in the communication cycle. The other 18 % is due to wasted time interval between backscatter packets.

The aggregate throughput of the network also increases linearly as the number of RX units and sensor nodes in the measurement increases. The measurement with sensor nodes placed at locations (1-5) achieves an aggregate throughput of 375 Kbps using 5 RX, which is 4.17 × faster than a single sensor node. This result shows that multiple backscatter sensor nodes can operate simultaneously and share the spectrum resources among themselves.

In cases where two close sensor nodes communicate with two different RX units, such as (7,8) and (9,10), we observe a lower aggregate throughput compared to the cases where sensor nodes are placed further away from each other, such as (2,3) or (7,10). Our analysis shows that this is mainly due to interference in waking up the sensor nodes since the sensor node wake-up radio uses amplitude modulation , which is more susceptible to interference. The second factor affecting the throughput is the interference caused by the carrier signals from other backscatter links. As the number of RX units increases, the number of simultaneous carrier signals
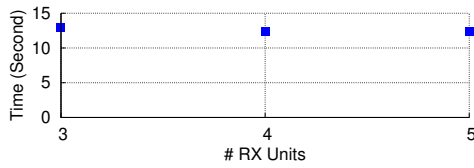
Figure 15: Handover duration.

increases too which contributes to data loss, especially where the sensors from multiple RX units are deployed near each other.

Although we test with a maximum of ten sensor nodes due to the limited hardware we have at our disposal, there is no strict limitation on the number of sensor nodes in the proposed network stack. We use 16-bit IDs for the sensor nodes in this work which limits the number of sensor nodes to 65535, but that limitation can be relaxed by using 32-bit IDs. In the current implementation, each backscatter cycle takes a minimum of 10ms. Therefore, each RX unit can communicate with up to 100 sensor nodes each second.

6.6 Handover

To demonstrate that MultiScatter can manage the movement of sensor nodes between RX units, we set up the system in an office building with three isolated rooms, walk within these rooms at an average pace while carrying the sensor node. We repeat the experiment 10 times for each scenario where the system uses 3, 4, and 5 RX units and 2 TX units for each RX unit. We use a threshold of 20 consecutive dropped packets in all three measurements.

Our results in Fig. 15 show that the average time difference between the last successfully received packet at the previous location and the first one at the new location is 13, 12.4, and 12.4 seconds when our setup has 3, 4, and 5 RX units, respectively. This time includes both the relocating time, 8.2 seconds on average, and assigning a new RX unit to the sensor node placed in the new location. This result suggests that the RX assignment process is not significant compared to the movement time in our experiments, and once the sensor node is settled in its new location, the network successfully reassigns it to a new RX unit.

7 RELATED WORK

Our work is related to prior efforts in backscatter communication, and battery-free sensing.

Backscatter Communication. Our work builds on recent efforts in advancing bistatic backscatter solutions to deliver ultra-low-power wireless connectivity. These efforts were focused on designing backscatter solutions compatible with existing wireless standards [23, 34, 38, 43, 46, 49, 58, 70, 83, 91, 92, 95], and improving backscatter throughput [42, 60, 97, 99], range [83, 87], reliability [46, 76] and deployability [36, 48]. While these works use a single RX-TX pair in their deployments, we use multiple RX and TX base units to realize wide area and scalable bistatic backscatter.

A wireless protocol to handle the concurrent transmission of backscatter devices was presented in [42], which uses chirp spread spectrum modulation to share the channel bandwidth between many devices communicating with a single monostatic backscatter access point. The access point can cover a wide area since each backscatter node has a low data rate that allows the backscattered signals to be recovered at very low signal powers. Using a single

access point is not a scalable solution. In this work, we use a network of backscatter base units to extend the coverage at data rates up to 250 Kbps. Although we use 802.15.4g standard with FSK modulation and time-division multiplexing in this work, the techniques presented can be combined with other modulation and multiple access methods.

A scalable backscatter sensor mesh was introduced in [96] that uses distributed excitation to enable multi-hop backscatter between sensor nodes. Although this solution enables the sensor nodes to communicate with each other at longer distances, it requires an excitation source close to each sensor node resulting in significant deployment limitations. In our architecture, the sensor nodes only communicate with the base units. The network of base units handles the tasks that allow the sensor nodes to move freely inside the coverage area without adding any complexity to the sensor nodes.

Battery-free sensing. Battery-free solutions rely on the harvested energy from RF [66, 67, 78, 80, 84], solar [31, 62, 88], vibration [57, 68], motion [82], thermal [62] and magnetic [40] energy sources for their operation. [94] lists mean energy generated by 50 activities in residential buildings. Applications such as video [41, 44, 78] and audio [84] streaming, gaming [31], full-body temperature mapping [40], food quality monitoring [73], pulse oximetry [51, 90], structural health monitoring [61], flying insects EMG telemetry [86], indoor acoustic localization [98], eye-tracking [56], visible light sensing [88] and many others [39, 53, 55, 59, 82] have been realized with battery-free platforms. In this work, we develop a modular battery-free sensing platform based on bistatic backscatter wireless communication, and use camera, microphone and environmental sensors as examples to show the platform capabilities.

8 CONCLUSION

We present the first wide-area multistatic backscatter network for battery-free wireless sensors. We discuss the limitations of backscatter systems, such as the limited coverage area, frequency-dependent operability, and sensor node limitations in handling network tasks. Our MAC layer implementation is designed to overcome these limitations by selecting the best RX-TX pair, carrier power, and frequency in communicating with each sensor to maximize the throughput and handling the handover between base units as the sensor moves inside the coverage area. We build low-cost hardware using COTS components and prototype proof-of-concept battery-free sensors for capturing images, audio, and environmental data.

This work is a first step toward, and a sample implementation of wide-area low-cost backscatter networks. There are many opportunities to improve the system in future work. Techniques such as joint sensing and communication, coherent transmission of carrier signals and detection of backscatter packets, localizing and tracking the movements of sensor nodes for faster hand over, and many more can be employed to further extend the throughput, coverage, and reliability, and reduce the energy consumption and latency of wide area multistatic backscatter networks.

REFERENCES

[1] 2006. *S463XX datasheet*. ftp://ftp2.nearson.com/Drawings/Antenna/S463XX-915.pdf
[2] 2008. *AS213-92LF datasheet*. https://www.skyworksinc.com/en/Products/switches/AS213-92LF
[3] 2012. *EKMB1104111 datasheet*. https://media.digikey.com/pdf/DataSheets/PanasonicSensorsPDFs/EKMB_MC_AMN2_3_Rev_Sep_2012.pdf
[4] 2015. *AS3933 datasheet*. https://www.sciosense.com/products/wireless-sensor-nodes/as3933-lf-receiver-ic/
[5] 2016. *Humidity & Temp Sensor Node for Star Networks Enabling 10+ Year Coin Cell Battery Life Ref Design*. https://www.ti.com/tool/TIDA-00374
[6] 2016. *OPT3002 datasheet*. https://www.ti.com/product/OPT3002
[7] 2017. *SKY65313-21 datashett*. https://www.skyworksinc.com/en/Products/Front-end-Modules/SKY65313-21 https://www.skyworksinc.com/en/Products/Front-end-Modules/SKY65313-21.
[8] 2019. *BQ25570 datasheet*. https://www.ti.com/product/BQ25570
[9] 2019. *Electronic Code of Federal Regulations, Title 47, Chapter I, Subchapter A, Part 15, Subpart C, section 15.247*. www.ecfr.gov www.ecfr.gov.
[10] 2019. *HDC2080 datasheet*. https://www.ti.com/product/HDC2080
[11] 2019. *Himax HM01B0*. https://www.himax.com.tw/products/cmos-image-sensor/image-sensors/hm01b0/
[12] 2019. *STM32L071CB datasheet*. https://www.st.com/resource/en/datasheet/stm32l071cb.pdf
[13] 2019. *VM1010 datasheet*. https://vespermems.com/products/vm1010/
[14] 2020. *100 mF supercapacitor catalog*. https://content.kemet.com/datasheets/KEM_S6015_FY.pdf
[15] 2020. *CC1312R datasheet*. https://www.ti.com/product/CC1312R https://www.ti.com/product/CC1312.
[16] 2020. *CC1352R datasheet*. https://www.ti.com/product/CC1352R https://www.ti.com/product/CC1310.
[17] 2020. *LTC6990 datasheet*. https://www.analog.com/media/en/technical-documentation/data-sheets/LTC6990.pdf
[18] 2020. *Panasonic solar panel catalog*. https://panasonic.co.jp/ls/psam/en/products/pdf/Catalog_Amorton_ENG.pdf
[19] 2021. *Python socket.io project*. https://pypi.org/project/python-socketio/
[20] 2021. *TAP Software*. https://www.softwright.com/
[21] 2021. *Wireless InSite 3D Wireless Prediction Software*. https://www.remcom.com/wireless-insite-em-propagation-software
[22] 2021. www.octopart.com.
[23] Ali Abedi, Mohammad Hossein Mazaheri, Omid Abari, and Tim Brecht. 2018. WiTAG: Rethinking Backscatter Communication for WiFi Networks. In *Proceedings of the 17th ACM Workshop on Hot Topics in Networks - HotNets '18*. ACM Press. https://doi.org/10.1145/3286062.3286084
[24] Rabe Arshad, Hesham ElSawy, Sameh Sorour, Tareq Y. Al-Naffouri, and Mohamed-Slim Alouini. 2016. Handover management in dense cellular networks: A stochastic geometry approach. In *2016 IEEE International Conference on Communications (ICC)*. IEEE. https://doi.org/10.1109/icc.2016.7510709
[25] Ari Asp, Yaroslav Sydorov, Mikko Keskikastari, Mikko Valkama, and Jarno Niemela. [n.d.]. Impact of Modern Construction Materials on Radio Signal Propagation: Practical Measurements and Network Planning Aspects. In *2014 IEEE 79th Vehicular Technology Conference (VTC Spring)* (2014-05). IEEE. https://doi.org/10.1109/vtcspring.2014.7022939
[26] Ari Asp, Yaroslav Sydorov, Mikko Valkama, and Jarno Niemela. [n.d.]. Radio signal propagation and attenuation measurements for modern residential buildings. In *2012 IEEE Globecom Workshops* (2012-12). IEEE. https://doi.org/10.1109/glocomw.2012.6477638
[27] Dinesh Bharadia, Kiran Raj Joshi, Manikanta Kotaru, and Sachin Katti. 2015. BackFi: High Throughput WiFi Backscatter. *ACM SIGCOMM Computer Communication Review* 45, 5 (aug 2015), 283–296. https://doi.org/10.1145/2829988.2787490
[28] Alberto Coustasse, M. Tomblin, and Chelsea Slack. 2013. Impact of Radio-Frequency Identification (RFID) Technologies on the Hospital Supply Chain: A Literature Review. *Perspectives in health information management / AHIMA, American Health Information Management Association* 10 (10 2013), 1d.
[29] Andrei Croitoru, Dragos Niculescu, and Costin Raiciu. 2015. Towards Wifi Mobility without Fast Handover. In *12th USENIX Symposium on Networked Systems Design and Implementation (NSDI 15)*. USENIX Association, Oakland, CA, 219–234. https://www.usenix.org/conference/nsdi15/technical-sessions/presentation/croitoru
[30] Jasper de Winkel, Carlo Delle Donne, Kasim Sinan Yildirim, Przemysław Pawełczak, and Josiah Hester. [n.d.]. Reliable Timekeeping for Intermittent Computing. In *Proceedings of the Twenty-Fifth International Conference on Architectural Support for Programming Languages and Operating Systems* (2020-03). ACM. https://doi.org/10.1145/3373376.3378464
[31] Jasper de Winkel, Vito Kortbeek, Josiah Hester, and Przemysław Pawełczak. 2020. Battery-Free Game Boy. *Proceedings of the ACM on Interactive, Mobile, Wearable and Ubiquitous Technologies* 4, 3 (sep 2020), 1–34. https://doi.org/10.1145/3411839

[32] Abhishekh Devaraj, Mohamed Megahed, Yutao Liu, Ashwin Ramachandran, and Tejasvi Anand. 2019. A Switched Capacitor Multiple Input Single Output Energy Harvester (Solar Piezo) Achieving 74.6% Efficiency With Simultaneous MPPT. *IEEE Transactions on Circuits and Systems I: Regular Papers* 66, 12 (dec 2019), 4876–4887. https://doi.org/10.1109/tcsi.2019.2934985
[33] Joshua F. Ensworth, Alexander T. Hoang, Thang Q. Phu, and Matthew S. Reynolds. 2017. Full-duplex Bluetooth Low Energy (BLE) compatible Backscatter communication system for mobile devices. In *2017 IEEE Topical Conference on Wireless Sensors and Sensor Networks (WiSNet)*. IEEE. https://doi.org/10.1109/wisnet.2017.7878752
[34] Joshua F. Ensworth and Matthew S. Reynolds. 2017. BLE-Backscatter: Ultralow-Power IoT Nodes Compatible With Bluetooth 4.0 Low Energy (BLE) Smartphones and Tablets. *IEEE Transactions on Microwave Theory and Techniques* 65, 9 (sep 2017), 3360–3368. https://doi.org/10.1109/tmtt.2017.2687866
[35] H.T. Friis. 1946. A Note on a Simple Transmission Formula. *Proceedings of the IRE* 34, 5 (may 1946), 254–256. https://doi.org/10.1109/jrproc.1946.234568
[36] Ander Galisteo, Ambuj Varshney, and Domenico Giustiniano. 2020. Two to tango: hybrid light and backscatter networks for next billion devices. In *Proceedings of the 18th International Conference on Mobile Systems, Applications, and Services*. ACM. https://doi.org/10.1145/3386901.3388918
[37] Kai Geissdoerfer and Marco Zimmerling. 2021. Bootstrapping Battery-free Wireless Networks: Efficient Neighbor Discovery and Synchronization in the Face of Intermittency. In *18th USENIX Symposium on Networked Systems Design and Implementation (NSDI 21)*. USENIX Association, 439–455. https://www.usenix.org/conference/nsdi21/presentation/geissdoerfer
[38] Wei Gong, Longzhi Yuan, Qiwei Wang, and Jia Zhao. 2020. Multiprotocol backscatter for personal IoT sensors. In *Proceedings of the 16th International Conference on emerging Networking EXperiments and Technologies*. ACM. https://doi.org/10.1145/3386367.3432883
[39] Philipp Gutruf, Rose T. Yin, K. Benjamin Lee, Jokubas Ausra, Jaclyn A. Brennan, Yun Qiao, Zhaoqian Xie, Roberto Peralta, Olivia Talarico, Alejandro Murillo, Sheena W. Chen, John P. Leshock, Chad R. Haney, Emily A. Waters, Changxing Zhang, Haiwen Luan, Yonggang Huang, Gregory Trachiotis, Igor R. Efimov, and John A. Rogers. 2019. Wireless, battery-free, fully implantable multimodal and multisite pacemakers for applications in small animal models. *Nature Communications* 10, 1 (dec 2019). https://doi.org/10.1038/s41467-019-13637-w
[40] Seungyong Han, Jeonghyun Kim, Sang Min Won, Yinji Ma, Daeshik Kang, Zhaoqian Xie, Kyu-Tae Lee, Ha Uk Chung, Anthony Banks, Seunghwan Min, Seung Yun Heo, Charles R. Davies, Jung Woo Lee, Chi-Hwan Lee, Bong Hoon Kim, Kan Li, Yadong Zhou, Chen Wei, Xue Feng, Yonggang Huang, and John A. Rogers. 2018. Battery-free, wireless sensors for full-body pressure and temperature mapping. *Science Translational Medicine* 10, 435 (apr 2018), eaan4950. https://doi.org/10.1126/scitranslmed.aan4950
[41] Mehrdad Hessar, Saman Naderiparizi, Ye Wang, Ali Saffari, Shyamnath Gollakota, and Joshua R. Smith. 2018. Wireless Video Streaming for Ultra-low-power Cameras. In *Proceedings of the 16th Annual International Conference on Mobile Systems, Applications, and Services*. ACM. https://doi.org/10.1145/3210240.3211109
[42] Mehrdad Hessar, Ali Najafi, and Shyamnath Gollakota. 2019. Netscatter: Enabling Large-scale Backscatter Networks. In *Proceedings of the 16th USENIX Conference on Networked Systems Design and Implementation* (Boston, MA, USA) *(NSDI'19)*. USENIX Association, Berkeley, CA, USA, 271–283. http://dl.acm.org/citation.cfm?id=3323234.3323258
[43] Vikram Iyer, Vamsi Talla, Bryce Kellogg, Shyamnath Gollakota, and Joshua Smith. 2016. Inter-Technology Backscatter: Towards Internet Connectivity for Implanted Devices. In *Proceedings of the 2016 ACM SIGCOMM Conference* (Florianopolis, Brazil) *(SIGCOMM '16)*. ACM, New York, NY, USA, 356–369. https://doi.org/10.1145/2934872.2934894
[44] Colleen Josephson, Lei Yang, Pengyu Zhang, and Sachin Katti. 2019. Wireless computer vision using commodity radios. In *Proceedings of the 18th International Conference on Information Processing in Sensor Networks - IPSN '19*. ACM Press. https://doi.org/10.1145/3302506.3310403
[45] Ramgopal Kashyap. 2020. Applications of Wireless Sensor Networks in Healthcare. In *Advances in Wireless Technologies and Telecommunication*. IGI Global, 8–40. https://doi.org/10.4018/978-1-5225-9004-0.ch002
[46] Mohamad Katanbaf, Vivek Jain, and Joshua R. Smith. 2020. Relacks: Reliable Backscatter Communication in Indoor Environments. *Proceedings of the ACM on Interactive, Mobile, Wearable and Ubiquitous Technologies* 4, 2 (jun 2020), 1–24. https://doi.org/10.1145/3397314
[47] Mohamad Katanbaf, Ali Saffari, and Joshua R. Smith. 2020. Receiver Selectivity Limits on Bistatic Backscatter Range. In *2020 IEEE International Conference on RFID (RFID)*. IEEE. https://doi.org/10.1109/rfid49298.2020.9244826
[48] Mohamad Katanbaf, Anthony Weinand, and Vamsi Talla. 2021. Simplifying Backscatter Deployment: Full-Duplex LoRa Backscatter. In *18th USENIX Symposium on Networked Systems Design and Implementation (NSDI 21)*. USENIX Association, 955–972. https://www.usenix.org/conference/nsdi21/presentation/katanbaf
[49] Bryce Kellogg, Vamsi Talla, Shyamnath Gollakota, and Joshua R. Smith. 2016. Passive Wi-Fi: Bringing Low Power to Wi-Fi Transmissions. In *Proceedings of the 13th Usenix Conference on Networked Systems Design and Implementation*

(Santa Clara, CA) (*NSDI'16*). USENIX Association, Berkeley, CA, USA, 151–164. http://dl.acm.org/citation.cfm?id=2930611.2930622

[50] Daeyoung Kim, M.A. Ingram, and W.W. Smith. 2003. Measurements of small-scale fading and path loss for long range RF tags. *IEEE Transactions on Antennas and Propagation* 51, 8 (aug 2003), 1740–1749. https://doi.org/10.1109/tap.2003.814752

[51] Jeonghyun Kim, Philipp Gutruf, Antonio M. Chiarelli, Seung Yun Heo, Kyoungyeon Cho, Zhaoqian Xie, Anthony Banks, Seungyoung Han, Kyung-In Jang, JungWoo Lee, Kyu-Tae Lee, Xue Feng, Yonggang Huang, Monica Fabiani, Gabriele Gratton, Ungyu Paik, and John A. Rogers. 2016. Miniaturized Battery-Free Wireless Systems for Wearable Pulse Oximetry. *Advanced Functional Materials* 27, 1 (nov 2016), 1604373. https://doi.org/10.1002/adfm.201604373

[52] David C. Klonoff and David Kerr. 2018. Smart Pens Will Improve Insulin Therapy. *Journal of Diabetes Science and Technology* 12, 3 (feb 2018), 551–553. https://doi.org/10.1177/1932296818759845

[53] Siddharth R. Krishnan, Chun-Ju Su, Zhaoqian Xie, Manish Patel, Surabhi R. Madhvapathy, Yeshou Xu, Juliet Freudman, Barry Ng, Seung Yun Heo, Heling Wang, Tyler R. Ray, John Leshock, Izabela Stankiewicz, Xue Feng, Yonggang Huang, Philipp Gutruf, and John A. Rogers. 2018. Wireless, Battery-Free Epidermal Electronics for Continuous, Quantitative, Multimodal Thermal Characterization of Skin. *Small* 14, 47 (oct 2018), 1803192. https://doi.org/10.1002/smll.201803192

[54] Antonio Lazaro, David Girbau, and David Salinas. 2009. Radio Link Budgets for UHF RFID on Multipath Environments. *IEEE Transactions on Antennas and Propagation* 57, 4 (apr 2009), 1241–1251. https://doi.org/10.1109/tap.2009.2015818

[55] Sanghoon Lee, Hao Wang, Jiahui Wang, Qiongfeng Shi, Shih-Cheng Yen, Nitish V. Thakor, and Chengkuo Lee. 2018. Battery-free neuromodulator for peripheral nerve direct stimulation. *Nano Energy* 50 (aug 2018), 148–158. https://doi.org/10.1016/j.nanoen.2018.04.004

[56] Tianxing Li and Xia Zhou. 2018. Battery-Free Eye Tracker on Glasses. In *Proceedings of the 24th Annual International Conference on Mobile Computing and Networking - MobiCom '18*. ACM Press. https://doi.org/10.1145/3241539.3241578

[57] Xin Li, Li Teng, Hong Tang, Jingying Chen, Haoyu Wang, Yu Liu, Minfan Fu, and Junrui Liang. 2020. ViPSN: A vibration-powered iot platform. *IEEE Internet of Things Journal* (2020).

[58] Yan Li, Zicheng Chi, Xin Liu, and Ting Zhu. 2018. Passive-ZigBee: Enabling ZigBee Communication in IoT Networks with 1000X+ Less Power Consumption. In *Proceedings of the 16th ACM Conference on Embedded Networked Sensor Systems - SenSys '18*. ACM Press. https://doi.org/10.1145/3274783.3274846

[59] Xiaoyou Lin and Boon-Chong Seet. 2017. Battery-Free Smart Sock for Abnormal Relative Plantar Pressure Monitoring. *IEEE Transactions on Biomedical Circuits and Systems* 11, 2 (apr 2017), 464–473. https://doi.org/10.1109/tbcas.2016.2615603

[60] Xin Liu, Zicheng Chi, Wei Wang, Yao Yao, and Ting Zhu. 2020. VMscatter: A Versatile MIMO Backscatter. In *17th USENIX Symposium on Networked Systems Design and Implementation (NSDI 20)*. 895–909.

[61] Gaël Loubet, Alexandru Takacs, Ethan Gardner, Andrea De Luca, Florin Udrea, and Daniela Dragomirescu. 2019. LoRaWAN Battery-Free Wireless Sensors Network Designed for Structural Health Monitoring in the Construction Domain. *Sensors* 19, 7 (mar 2019), 1510. https://doi.org/10.3390/s19071510

[62] Michele Magno, Xiaying Wang, Manuel Eggimann, Lukas Cavigelli, and Luca Benini. 2020. InfiniWolf: Energy Efficient Smart Bracelet for Edge Computing with Dual Source Energy Harvesting. In *2020 Design, Automation & Test in Europe Conference & Exhibition (DATE)*. IEEE. https://doi.org/10.23919/date48585.2020.9116218

[63] Vivek Mangal and Peter R. Kinget. 2019. 28.1 A 0.42nW 434MHz -79.1dBm Wake-Up Receiver with a Time-Domain Integrator. In *2019 IEEE International Solid-State Circuits Conference - (ISSCC)*. IEEE. https://doi.org/10.1109/isscc.2019.8662418

[64] Joseph Mauro, Kelly B. Mathews, and Eric S. Sredzinski. 2019. Effect of a Smart Pill Bottle and Pharmacist Intervention on Medication Adherence in Patients with Multiple Myeloma New to Lenalidomide Therapy. *Journal of Managed Care & Specialty Pharmacy* 25, 11 (nov 2019), 1244–1254. https://doi.org/10.18553/jmcp.2019.25.11.1244

[65] Hannes Michaels, Michael Rinderle, Richard Freitag, Iacopo Benesperi, Tomas Edvinsson, Richard Socher, Alessio Gagliardi, and Marina Freitag. 2020. Dye-sensitized solar cells under ambient light powering machine learning: towards autonomous smart sensors for the internet of things. *Chemical Science* 11, 11 (2020), 2895–2906. https://doi.org/10.1039/c9sc06145b

[66] Timothy Miller, Stephen S Oyewobi, Adnan M Abu-Mahfouz, and Gerhard P Hancke. 2020. Enabling a Battery-Less Sensor Node Using Dedicated Radio Frequency Energy Harvesting for Complete Off-Grid Applications. *Energies* 13, 20 (2020), 5402.

[67] Saman Naderiparizi, Aaron N. Parks, Zerina Kapetanovic, Benjamin Ransford, and Joshua R. Smith. 2015. WISPCam: A battery-free RFID camera. In *2015 IEEE International Conference on RFID (RFID)*. IEEE. https://doi.org/10.1109/rfid.2015.7113088

[68] Francesco Orfei, Chiara Benedetta Mezzetti, and Francesco Cottone. 2016. Vibrations powered LoRa sensor: An electromechanical energy harvester working on a real bridge. In *2016 IEEE SENSORS*. IEEE. https://doi.org/10.1109/icsens.2016.7808752

[69] Christoph Paasch, Gregory Detal, Fabien Duchene, Costin Raiciu, and Olivier Bonaventure. 2012. Exploring mobile/WiFi handover with multipath TCP. In *Proceedings of the 2012 ACM SIGCOMM workshop on Cellular networks: operations, challenges, and future design - CellNet '12*. ACM Press. https://doi.org/10.1145/2342468.2342476

[70] Yao Peng, Longfei Shangguan, Yue Hu, Yujie Qian, Xianshang Lin, Xiaojiang Chen, Dingyi Fang, and Kyle Jamieson. 2018. PLoRa: a passive long-range data network from ambient LoRa transmissions. In *Proceedings of the 2018 Conference of the ACM Special Interest Group on Data Communication - SIGCOMM 18*. ACM Press. https://doi.org/10.1145/3230543.3230567

[71] G.P. Pollini. 1996. Trends in handover design. *IEEE Communications Magazine* 34, 3 (mar 1996), 82–90. https://doi.org/10.1109/35.486807

[72] Poonam, Kriti Sharma, Anmol Arora, and S.K. Tripathi. 2019. Review of supercapacitors: Materials and devices. *Journal of Energy Storage* 21 (feb 2019), 801–825. https://doi.org/10.1016/j.est.2019.01.010

[73] Radislav A. Potyrailo, Nandini Nagraj, Zhexiong Tang, Frank J. Mondello, Cheryl Surman, and William Morris. 2012. Battery-free Radio Frequency Identification (RFID) Sensors for Food Quality and Safety. *Journal of Agricultural and Food Chemistry* 60, 35 (aug 2012), 8535–8543. https://doi.org/10.1021/jf302416y

[74] Anthony Quelen, Gael Pillonnet, Pierre Gasnier, Francois Rummens, and Sebastien Boisseau. 2020. 32.3 Electromagnetic Mechanical Energy-Harvester IC with No Off-Chip Component and One Switching Period MPPT Achieving up to 95.9% End-to-End Efficiency and 460% Energy-Extraction Gain. In *2020 IEEE International Solid- State Circuits Conference - (ISSCC)*. IEEE. https://doi.org/10.1109/isscc19947.2020.9063023

[75] Ignacio Rodriguez, Huan C. Nguyen, Niels T. K. Jorgensen, Troels B. Sorensen, and Preben Mogensen. [n.d.]. Radio Propagation into Modern Buildings: Attenuation Measurements in the Range from 800 MHz to 18 GHz. In *2014 IEEE 80th Vehicular Technology Conference (VTC2014-Fall)* (2014-09). IEEE. https://doi.org/10.1109/vtcfall.2014.6966147

[76] Mohammad Rostami, Jeremy Gummeson, Ali Kiaghadi, and Deepak Ganesan. 2018. Polymorphic Radios: A New Design Paradigm for Ultra-low Power Communication. In *Proceedings of the 2018 Conference of the ACM Special Interest Group on Data Communication* (Budapest, Hungary) (*SIGCOMM '18*). ACM, New York, NY, USA, 446–460. https://doi.org/10.1145/3230543.3230571

[77] Kamala Raghavan Sadagopan, Jian Kang, Sanket Jain, Yogesh Ramadass, and Arun Natarajan. 2017. A 365nW -61.5 dBm sensitivity, 1.875 cm2 2.4 GHz wake-up receiver with rectifier-antenna co-design for passive gain. In *2017 IEEE Radio Frequency Integrated Circuits Symposium (RFIC)*. IEEE. https://doi.org/10.1109/rfic.2017.7969047

[78] Ali Saffari, Mehrdad Hessar, Saman Naderiparizi, and Joshua R. Smith. 2019. Battery-Free Wireless Video Streaming Camera System. In *2019 IEEE International Conference on RFID (RFID)*. IEEE. https://doi.org/10.1109/rfid.2019.8719264

[79] Ali Saffari, Sin Yong Tan, Mohamad Katanbaf, Homagni Saha, Joshua R. Smith, and Soumik Sarkar. 2021. Battery-Free Camera Occupancy Detection System. In *Proceedings of the 5th International Workshop on Embedded and Mobile Deep Learning* (Virtual, WI, USA) (*EMDL'21*). Association for Computing Machinery, New York, NY, USA, 13–18. https://doi.org/10.1145/3469116.3470013

[80] A.P. Sample, D.J. Yeager, P.S. Powledge, A.V. Mamishev, and J.R. Smith. 2008. Design of an RFID-Based Battery-Free Programmable Sensing Platform. *IEEE Transactions on Instrumentation and Measurement* 57, 11 (nov 2008), 2608–2615. https://doi.org/10.1109/tim.2008.925019

[81] Lukas Sigrist, Rehan Ahmed, Andres Gomez, and Lothar Thiele. 2020. Harvesting-Aware Optimal Communication Scheme for Infrastructure-Less Sensing. *ACM Trans. Internet Things* 1, 4, Article 22 (June 2020), 26 pages. https://doi.org/10.1145/3395928

[82] Yu Song, Jihong Min, You Yu, Haobin Wang, Yiran Yang, Haixia Zhang, and Wei Gao. 2020. Wireless battery-free wearable sweat sensor powered by human motion. *Science Advances* 6, 40 (sep 2020), eaay9842. https://doi.org/10.1126/sciadv.aay9842

[83] Vamsi Talla, Mehrdad Hessar, Bryce Kellogg, Ali Najafi, Joshua R. Smith, and Shyamnath Gollakota. 2017. LoRa Backscatter: Enabling The Vision of Ubiquitous Connectivity. *Proceedings of the ACM on Interactive, Mobile, Wearable and Ubiquitous Technologies* 1, 3 (sep 2017), 1–24. https://doi.org/10.1145/3130970

[84] Vamsi Talla, Bryce Kellogg, Shyamnath Gollakota, and Joshua R. Smith. 2017. Battery-Free Cellphone. *Proceedings of the ACM on Interactive, Mobile, Wearable and Ubiquitous Technologies* 1, 2 (jun 2017), 1–20. https://doi.org/10.1145/3090090

[85] Vamsi Talla, Joshua Smith, and Shyamnath Gollakota. [n.d.]. Advances and Open Problems in Backscatter Networking. 24, 4 ([n.d.]), 32–38. https://doi.org/10.1145/3457356.3457367

[86] S. J. Thomas, R. R. Harrison, A. Leonardo, and M. S. Reynolds. 2012. A Battery-Free Multichannel Digital Neural/EMG Telemetry System for Flying Insects. *IEEE Transactions on Biomedical Circuits and Systems* 6, 5 (oct 2012), 424–436. https://doi.org/10.1109/tbcas.2012.2222881

[87] Ambuj Varshney, Carlos Pérez-Penichet, Christian Rohner, and Thiemo Voigt. 2017. LoRea: A Backscatter Architecture that Achieves a Long Communication Range. In *Proceedings of the 15th ACM Conference on Embedded Network Sensor Systems - SenSys 17*. ACM Press. https://doi.org/10.1145/3131672.3136996

[88] Ambuj Varshney, Andreas Soleiman, Luca Mottola, and Thiemo Voigt. 2017. Battery-free Visible Light Sensing. In *Proceedings of the 4th ACM Workshop on Visible Light Communication Systems*. ACM. https://doi.org/10.1145/3129881.3129890

[89] Po-Han Peter Wang, Chi Zhang, Hongsen Yang, Dinesh Bharadia, and Patrick P. Mercier. 2020. 20.1 A 28 W IoT Tag That Can Communicate with Commodity WiFi Transceivers via a Single-Side-Band QPSK Backscatter Communication Technique. In *2020 IEEE International Solid- State Circuits Conference - (ISSCC)*. IEEE. https://doi.org/10.1109/isscc19947.2020.9063133

[90] Hao Zhang, Philipp Gutruf, Kathleen Meacham, Michael C. Montana, Xingyue Zhao, Antonio M. Chiarelli, Abraham Vázquez-Guardado, Aaron Norris, Luyao Lu, Qinglei Guo, Chenkai Xu, Yixin Wu, Hangbo Zhao, Xin Ning, Wubin Bai, Irawati Kandela, Chad R. Haney, Debashis Chanda, Robert W. Gereau, and John A. Rogers. 2019. Wireless, battery-free optoelectronic systems as subdermal implants for local tissue oximetry. *Science Advances* 5, 3 (mar 2019), eaaw0873. https://doi.org/10.1126/sciadv.aaw0873

[91] Pengyu Zhang, Colleen Josephson, Dinesh Bharadia, and Sachin Katti. 2017. FreeRider: Backscatter Communication Using Commodity Radios. In *Proceedings of the 13th International Conference on emerging Networking and Technologies - CoNEXT17*. ACM Press. https://doi.org/10.1145/3143361.3143374

[92] Pengyu Zhang, Mohammad Rostami, Pan Hu, and Deepak Ganesan. 2016. Enabling Practical Backscatter Communication for On-body Sensors. In *Proceedings of the 2016 conference on ACM SIGCOMM 2016 Conference - SIGCOMM '16*. ACM Press. https://doi.org/10.1145/2934872.2934901

[93] Sanliang Zhang and Ning Pan. 2014. Supercapacitors Performance Evaluation. *Advanced Energy Materials* 5, 6 (dec 2014), 1401401. https://doi.org/10.1002/aenm.201401401

[94] Yang Zhang, Yasha Iravantchi, Haojian Jin, Swarun Kumar, and Chris Harrison. 2019. Sozu: Self-Powered Radio Tags for Building-Scale Activity Sensing. In *Proceedings of the 32nd Annual ACM Symposium on User Interface Software and Technology*. ACM. https://doi.org/10.1145/3332165.3347952

[95] Jia Zhao, Wei Gong, and Jiangchuan Liu. 2018. Spatial Stream Backscatter Using Commodity WiFi. In *Proceedings of the 16th Annual International Conference on Mobile Systems, Applications, and Services - MobiSys 18*. ACM Press. https://doi.org/10.1145/3210240.3210329

[96] Jia Zhao, Wei Gong, and Jiangchuan Liu. 2020. Towards scalable backscatter sensor mesh with decodable relay and distributed excitation. In *Proceedings of the 18th International Conference on Mobile Systems, Applications, and Services*. ACM. https://doi.org/10.1145/3386901.3388942

[97] Renjie Zhao, Fengyuan Zhu, Yuda Feng, Siyuan Peng, Xiaohua Tian, Hui Yu, and Xinbing Wang. 2019. OFDMA-Enabled Wi-Fi Backscatter. In *The 25th Annual International Conference on Mobile Computing and Networking - MobiCom 19*. ACM Press. https://doi.org/10.1145/3300061.3300121

[98] Yi Zhao and Joshua R. Smith. 2013. A battery-free RFID-based indoor acoustic localization platform. In *2013 IEEE International Conference on RFID (RFID)*. IEEE. https://doi.org/10.1109/rfid.2013.6548143

[99] Fengyuan Zhu, Yuda Feng, Qianru Li, Xiaohua Tian, and Xinbing Wang. 2020. DigiScatter: efficiently prototyping large-scale OFDMA backscatter networks. In *Proceedings of the 18th International Conference on Mobile Systems, Applications, and Services*. ACM. https://doi.org/10.1145/3386901.3388914